



Reconnaissance and learning after the February 6, 2018, earthquake in Hualien, Taiwan

Jui-Liang Lin¹ · Chun-Hsiang Kuo¹ · Yu-Wen Chang¹ · Shu-Hsien Chao¹ · Yi-An Li¹ · Wen-Cheng Shen¹ · Chung-Han Yu¹ · Cho-Yen Yang¹ · Fan-Ru Lin¹ · Hsiao-Hui Hung¹ · Chun-Chung Chen¹ · Chin-Kuo Su¹ · Shang-Yi Hsu¹ · Chih-Chieh Lu¹ · Lap-Loi Chung¹ · Shyh-Jiann Hwang¹

Received: 28 January 2020 / Accepted: 21 May 2020
© Springer Nature B.V. 2020

Abstract

An earthquake with an epicenter offshore of Hualien City in eastern Taiwan occurred at midnight on February 6, 2018. The Richter magnitude (M_L) of the earthquake was 6.26 and the seismic intensity ranged up to level VII, the strongest seismic intensity level regulated in Taiwan. Almost all the major damage resulting from this seismic event was occurred near both sides of the Milun Fault, where records from nearby strong motion stations displayed the characteristics of near-fault ground motions. The main seismic damage was the collapse of four buildings with soft bottom stories, one of which resulted in fourteen of the seventeen total fatalities. Comparing the acceleration response spectra with the design response spectra sheds light on the effects of near-fault ground motions on the collapsed buildings. Based on the eventual forms of collapsed buildings, building collapses that have generally led to major casualties in past seismic events around the world can be classified into sit-down, knee-down and lie-down types. In addition to the four collapsed buildings, seismic reconnaissance on other buildings, bridges, ports, and non-structural components have also been conducted. This study explores the issues and challenges arising from the reconnaissance results and thereby enhances learning from the seismic event.

Keywords Seismic reconnaissance · 0206 Hualien earthquake · Milun fault · Near-fault ground motion · Building collapse · Bridge · Liquefaction · Non-structural component

1 Introduction

By coincidence, the Hualien earthquake examined in this paper occurred exactly two years after the Meinong earthquake, which struck southern Taiwan on February 6, 2016 (Henry et al. 2017). Because the suffering caused by the 2016 Meinong earthquake was still vivid, the 2018 Hualien earthquake resulted in panic and attracted overwhelming attention across

✉ Jui-Liang Lin
jllin@ncree.narl.org.tw

¹ National Center for Research on Earthquake Engineering, 200, Section 3, Xinhai Rd, Taipei 106, Taiwan, R.O.C.

the nation. In order to examine the seismic damage states before they could be altered by rescue and restoration efforts, Taiwan’s National Center for Research on Earthquake Engineering (NCREE) sent its first reconnaissance team to Hualien City in the early morning of February 7, 2018. The seismic reconnaissance team collected information on the geology and damage states of buildings, non-structural components, bridges, and ports. This paper reports on their findings.

2 Ground motion characteristics

2.1 Overview

According to Taiwan’s Central Weather Bureau (CWB), this earthquake event occurred on February 6, 2018, at 23:50 local time (GMT + 8). The Richter magnitude (M_L) was 6.26. The epicenter was at 24.1° N, 121.73° E, approximately 20 km off Taiwan’s east coast and close to Hualien City. The depth of the hypocenter was 6.31 km. The observed peak ground acceleration (PGA) was 594 cm/s^2 at the strong motion station HWA057, which is 12.7 km away from the epicenter. The observed peak ground velocity (PGV) was 146 cm/s at the strong motion station HWA014, which is 19.1 km away from the epicenter. The PGAs of five strong motion stations reached Taiwan’s strongest intensity level VII (i.e., $\text{PGA} > 400 \text{ gal}$). Additionally, there were ten strong motion stations with PGVs greater than 75 cm/s.

Based on 101 CWB and 32 NCREE strong motion stations, Fig. 1a–c show the maps of PGA, spectral acceleration at 0.3 s (denoted by $S_a(T=0.3 \text{ s})$) divided by 2.5, and spectral acceleration at 1.0 s (denoted by $S_a(T=1.0 \text{ s})$), respectively. Based on Taiwan’s building seismic design code (CPAMI 2011), the effective peak acceleration (EPA) is defined as $0.4S_{DS}$, where S_{DS} is the designed spectral acceleration at short period. Therefore, Fig. 1b showing $S_a(T=0.3 \text{ s})/2.5$, which is the spectral acceleration at short period divided by 2.5 (i.e., multiplied by 0.4), attempts to reflect the EPA of this seismic event. Figure 2a–c are magnified plots of Fig. 1a–c, respectively, for the Hualien area. Figure 2a indicates that, besides the area near the epicenter, the Milun Fault is another area with high PGAs.

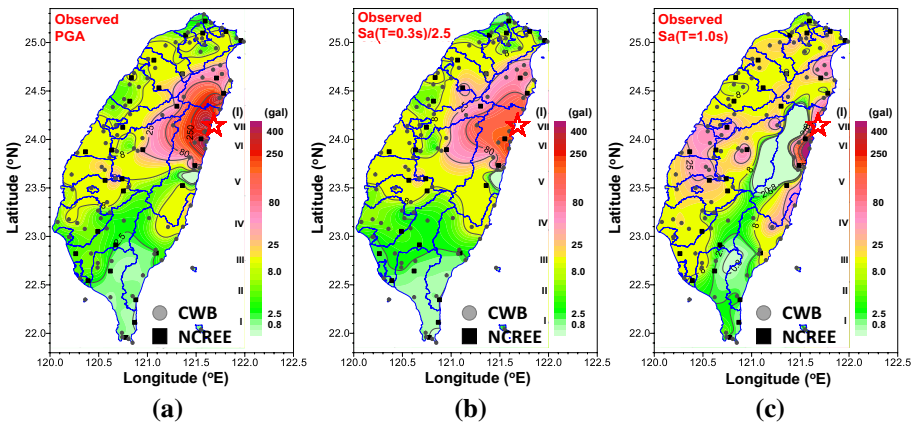


Fig. 1 Maps of a PGA, b $S_a(T=0.3 \text{ s})/2.5$, and c $S_a(T=1.0 \text{ s})$ across Taiwan

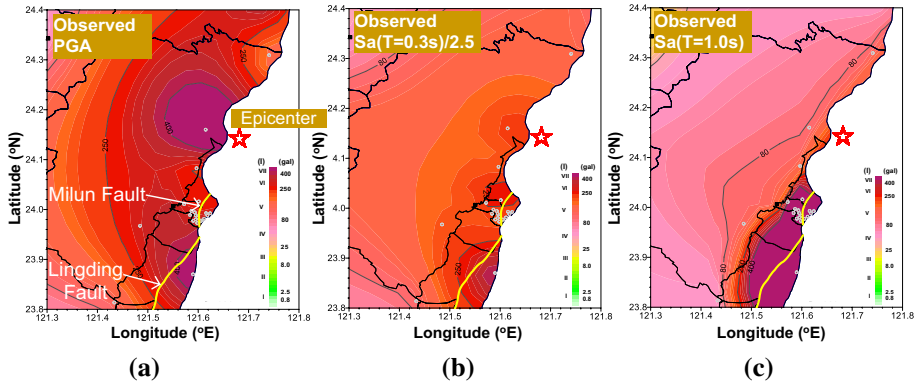


Fig. 2 Magnified maps of **a** PGA, **b** $S_a(T=0.3\text{ s})/2.5$, and **c** $S_a(T=1.0\text{ s})$ of the Hualien area

Moreover, the area with $S_a(T=1.0\text{ s})$ larger than 400 cm/s^2 only occurred along both sides of the Milun Fault and the Lingding Fault (Fig. 2c).

Accordingly, it is reasonable to expect that the earthquake would have more significantly affected the mid-rise buildings located on the two sides of the Milun Fault compared with those located in other areas. In fact, Taiwan’s Central Geological Survey (CGS 2018) reported that all the serious seismic damages in Hualien City were approximately located within the geologically sensitive zone of the Milun Fault, i.e., the 300-m-wide strip along the Milun Fault. In addition, some ruptures and dislocations on the ground surface along the Milun Fault were observed. Thus, it was confirmed that the Milun Fault was dislocated in this seismic event.

Table 1 lists the data of the strong motion stations with seismic intensity equal to or greater than level VI (i.e., $\text{PGA} \geq 250\text{ gal}$). Among the eighteen strong motion stations listed in Table 1, there are seven stations (i.e., HWA009, HWA011, HWA012, HWA013, HWA014, HWA028, and HWA050) with vertical PGAs greater than both the horizontal PGAs. In addition, all the PGVs of these seven stations are beyond 60 cm/s . As for the other stations, as long as the PGVs are significant, their vertical PGAs are close to their horizontal PGAs. Therefore, it is reasonable to infer that the reduced horizontal PGAs reflect the effect of soil nonlinearity. Further discussion on soil nonlinearity can be found from Kuo et al. (2019).

2.2 Characteristics of near-fault ground motion

Based on the pulse indicator proposed by Shahi and Baker (2014), the velocity histories recorded at the strong motion stations near the Milun Fault were analyzed to determine whether the ground motion records possess the characteristics of near-fault velocity pulses. The green arrows shown in Fig. 3 represent the magnitudes and directions of the velocity pulses observed at 17 strong motion stations (Table 2) in the Hualien area. In addition, the three contours of the PGVs equal to 40 cm/s , 80 cm/s , and 120 cm/s are also illustrated. Figure 3 indicates that all the records of the strong motion stations near the Milun Fault exhibit velocity pulses, most of which are toward the E-W direction, i.e., perpendicular to the Milun Fault. Figure 4 shows the velocity histories of strong motion stations HWA014

Table 1 Data of the strong motion stations with seismic intensity equal to or greater than level VI (i.e., $PGA \geq 250$ gal)

Station no	Longitude	Latitude	V_{S30} *	PGA-E/N/Z	PGV-E/N/Z
HWA057	121.6230	24.1587	815	243/594/173	8/11/3
HWA060	121.6017	23.9035	556	478/463/281	54/61/36
ILA050	121.7490	24.4258	627	245/432/86	7/9/2
HWA028	121.6095	24.0143	405	275/253/415	35/69/18
HWA019	121.6135	23.9750	504	403/370/213	132/92/34
HWA014	121.6057	23.9712	280	317/219/397	152/58/23
HWA012	121.6313	23.9920	410	280/281/338	66/57/25
HWA050	121.5908	23.9878	343	279/198/337	56/64/27
HWA008	121.6030	23.9873	297	230/336/331	93/97/33
HWA011	121.5948	23.9953	361	248/199/327	51/73/24
HWA013	121.5985	23.9755	337	316/220/324	91/55/33
HWA009	121.6223	23.9903	461	250/262/318	80/68/22
HWA010	121.6027	23.9783	250	314/197/283	116/69/33
HWA048	121.5805	24.0095	350	205/303/271	30/32/17
HWA058	121.4928	23.9658	526	261/302/159	13/10/9
HWA007	121.6262	23.9865	379	289/244/260	75/68/26
HWA063	121.5930	23.9935	289	216/253/253	49/79/25
A210	121.5587	24.0046	na	348/340/198	19/17/15

* V_{S30} is the average shear-wave velocity between 0 and 30-m depth

Fig. 3 Magnitudes and directions of the velocity pulses observed at the strong motion stations in the Hualien area

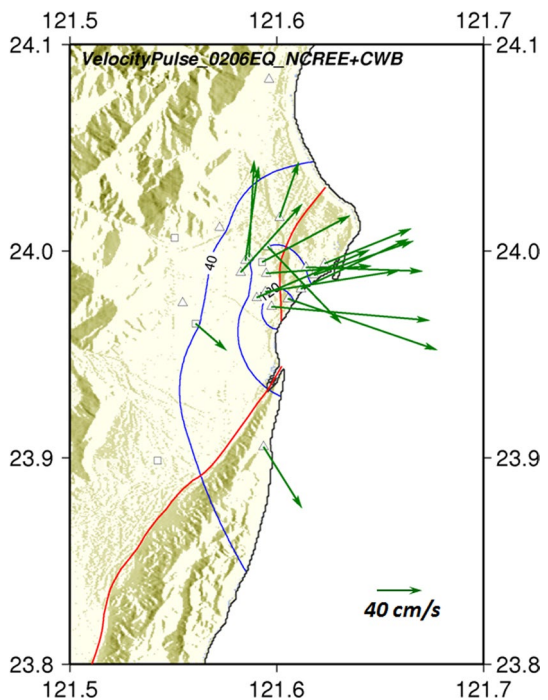


Table 2 V_{S30} and basic ground motion intensity measures of the 17 stations that recorded pulse-like velocities

Station code	V_{S30} (m/s)	PGA (gal)	PGV (cm/s)	V/H _{PGA}	R_{hypo} (km)	R_{rup} (km)
HWA007	379*	289.02	74.85	1.12	17.6	1.7
HWA008	297.03	336.48	97.19	1.25	19.0	0.7
HWA009	461*	317.55	80.12	1.34	17.5	1.3
HWA010	249.68	313.98	116.25	1.16	19.7	0.7
HWA011	360.84	327.11	72.57	1.48	19.1	1.6
HWA012	409.78	338.37	65.98	1.35	16.8	2.1
HWA013	336.76	323.62	90.53	1.41	20.2	1.2
HWA014	279.96	348.27	146.46	1.87	20.1	0.5
HWA019	503.52	403.00	138.39	0.70	19.3	0.3
HWA028	404.91	414.84	68.66	1.56	16.7	0.9
HWA050	343*	336.94	64.08	1.61	19.9	1.9
HWA060	556*	477.89	61.15	0.62	26.2	1.5
HWA062	605.69	213.80	88.32	1.09	18.5	1.0
HWA063	289*	253.40	78.68	1.18	19.3	1.7
TRB042	–	219.17	80.10	1.19	18.1	0.9
S009	–	304.97	94.72	0.93	18.8	0.9
S019	579.60	219.03	36.83	1.47	23.2	4.2

* Estimated V_{S30} from Kwok et al. (2018) and Lin et al. (2014)

V/H_{PGA}: The ratio of vertical PGA to horizontal PGA

R_{hypo} : The distance from the stations to the hypocenter

R_{rup} : The distance from the stations to Milun Fault

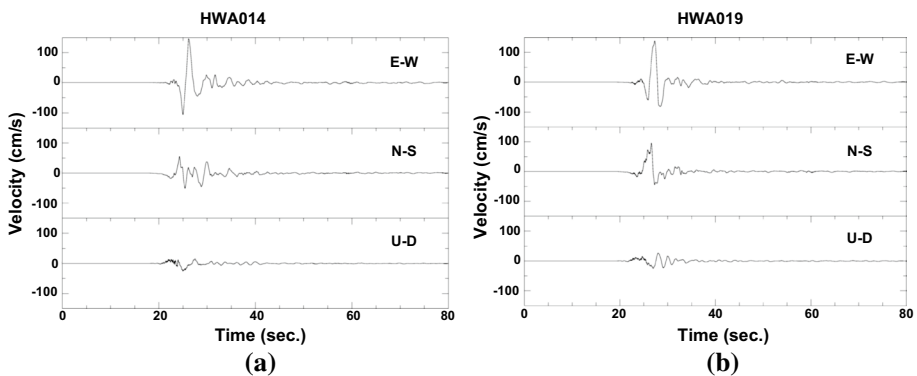


Fig. 4 Velocity histories of strong motion stations **a** HWA014 and **b** HWA019. From top to bottom, the plots show velocities in the E–W, N–S, and U–D directions

and HWA019, whose PGVs, the greatest two of all strong motion stations, are greater than 120 cm/s.

Figure 5a shows the distribution of the strong motion stations with PGA greater than 300 cm/s². Their acceleration response spectra are compared with the 475- and

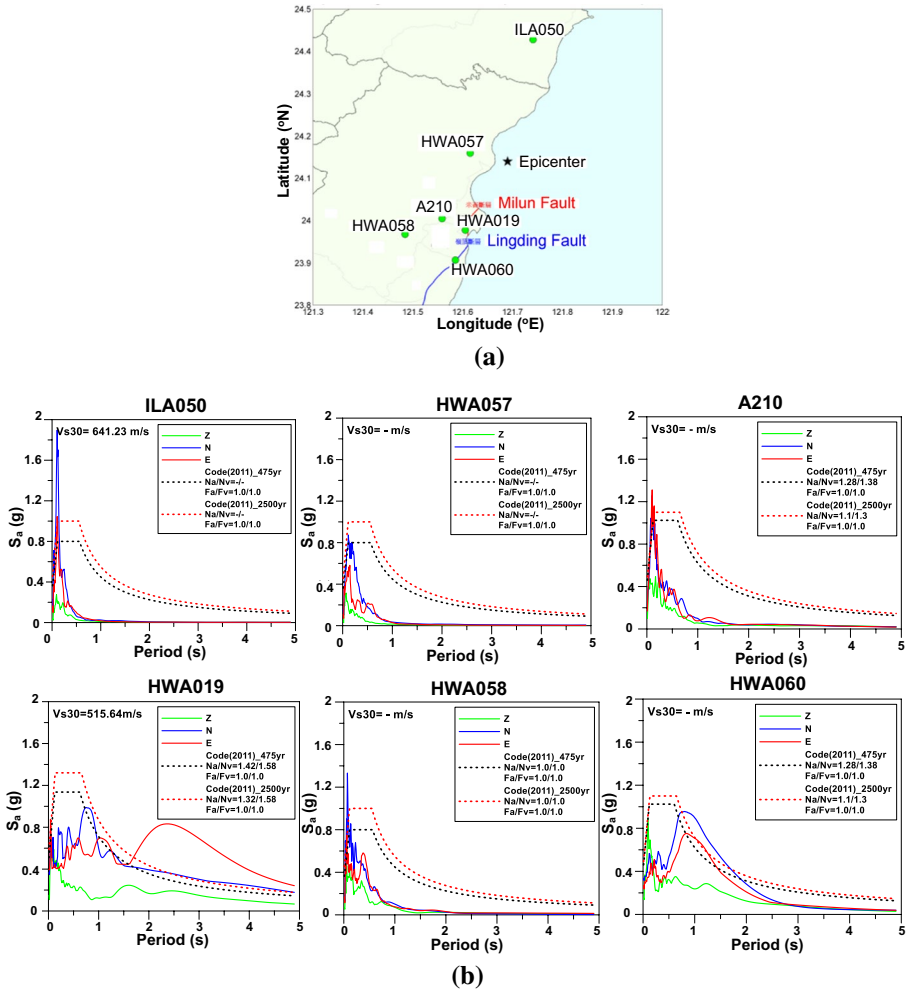


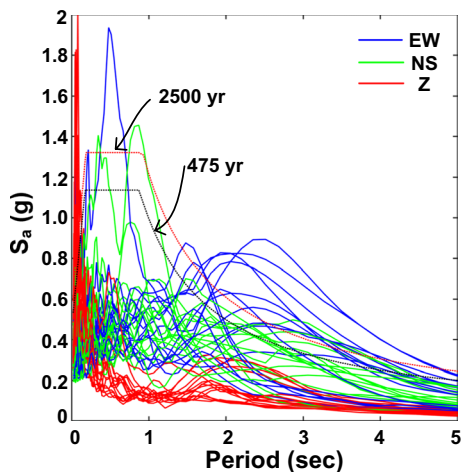
Fig. 5 **a** Distributions of the strong motion stations with PGA greater than 300 cm/s^2 and **b** their acceleration response spectra compared with the 475- and 2500-year-return-period design response spectra

2500-year-return-period design response spectra in Fig. 5b. Since 2005, Taiwan’s Building Seismic Design Code (CPAMI 2011) has considered near-fault effects by multiplying the design ground accelerations of the constant-acceleration region and the constant-velocity region by near-fault adjusting factors N_A and N_V , respectively. The values of the factors N_A and N_V , which decrease with distance between the site of interest and the fault, are shown in Fig. 5b. Additionally, the notations F_a and F_v shown in Fig. 5b are the site amplification factors for the design ground accelerations of the constant-acceleration region and of the constant-velocity region, respectively. The site conditions, which are determined by V_{S30} , at the strong motion stations across Taiwan have been investigated and compiled by NCREE (Kuo et al. 2012, 2017). Figure 5b indicates that the spectral accelerations at 2.5 s and 1.0 s of the response spectra of strong motion stations HWA019 and HWA060, respectively, have a significant peak. It is worth

noting that the distances of HWA019 and HWA060 to the ground surface of the fault are 0.5 km and 6.8 km, respectively. In addition, the site classes of the two stations HWA019 and HWA060 belong to the stiff site ($V_{S30} \geq 270$ m/s). Therefore, it is obvious that HWA019's and HWA060's spectral acceleration peaks at medium to long periods are due to the near-fault effects. The aforementioned spectral acceleration peaks, which are relatively larger than the corresponding values of the design response spectra with a 2500-year return period, imply that the medium-to-high-rise building structures around the two strong motion stations are likely to be seriously damaged. In contrast, the acceleration response spectra of the other four strong motion stations (i.e., ILA050, A210, HWA057, and HWA058) have peaks at short periods. Some of these peaks are larger than the corresponding values of the design response spectra with 475- or 2500-year return periods. It is thus reasonable to expect that some slight to medium damages might occur in low-rise buildings located around these four stations.

Figure 6 illustrates the acceleration response spectra of all three components of the ground acceleration records that have velocity pulses (Shahi and Baker 2014) recorded at the 17 strong motion stations (Table 2) (Kuo et al. 2019). The most conservative 475- and 2500-year-return-period design response spectra that consider a soft site ($V_{S30} \leq 180$ m/s) and near-fault distances less than 2 km are also illustrated in Fig. 6. The peaks of the E-W acceleration response spectra between 1.5 s and 2.5 s are substantially higher than the most conservative design response spectra. This implies that Taiwan's associated seismic design codes and policies of land exploitation need to be reviewed. For instance, in addition to the adequacy of the seismic design force considering the near-fault effects, the possible restriction on constructing buildings with fifteen or more stories in the near-fault areas are worth further examination. Moreover, it is worth referring the previous subsection's statement that the vertical PGAs of the strong motion stations in Hualien City were either close to or greater than their horizontal PGAs (Table 1). Accordingly, the current seismic design code's stipulation that the design vertical acceleration for buildings in near-fault areas is 2/3 of the corresponding horizontal acceleration appears to be inappropriate for this seismic event.

Fig. 6 Acceleration response spectra of all three components of the ground acceleration records that have velocity pulses



3 Buildings

The Hualien earthquake resulted in four buildings collapsing and one being seriously damaged. The four collapsed buildings were a 12-story mixed-use apartment block, a 6-story apartment building, a 9-story apartment building, and an 11-story hotel. The seriously damaged building was a 12-story department store. The collapsed buildings, all of which were constructed before 1999 Chi-Chi earthquake, had soft bottom stories and were located along the Milun Fault (Fig. 7). Because Taiwan's near-fault provisions were enacted in 2005, the design procedures at the times of construction of the four collapsed buildings did not include the near-fault provisions. Besides the four collapsed buildings, Fig. 7 also shows the location of a damaged bridge crossing the Milun Fault. The findings of the reconnaissance survey of the five buildings in addition to a base-isolated building and school buildings are stated as follows.

3.1 Collapsed 12-story mixed-use apartment

The collapse of this 12-story reinforced concrete (RC) building resulted in the severest number of fatalities, i.e., fourteen out of the total of seventeen in this earthquake. Figure 8a, b respectively show the front and rear sides of the collapsed building, which was built in 1994. The yellow steel struts shown in Fig. 8a are temporary measures to prevent the building from further collapse, which might threaten the lives of the rescuers. The floor plan of the building (Fig. 8c) indicates that the front of the building is to the south-west. In addition, the building is relatively plan-asymmetric. Due to the significantly high peaks of the E-W acceleration response spectra between 1.5 s and 2.5 s (Fig. 6), the building whose dominant vibration period was highly likely within the stated period range collapsed toward the front (i.e., the south-west direction). It is worth noting that the first and second stories of the building were commercially used as a hotel with large open spaces in its lobby/reception hall. Figure 8d–f show the damaged columns that had overly large spacing of stirrups, which was approximately equal to 25 cm to 30 cm. In addition, the splices of all the column reinforcements appeared at the same height (Fig. 8f), which was contrary to the

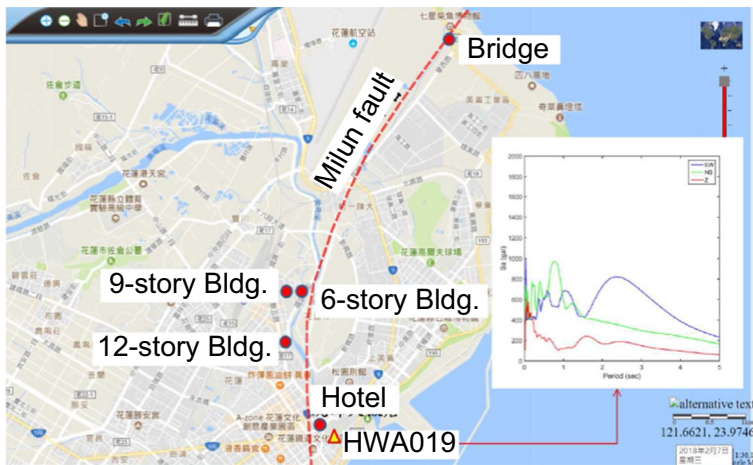


Fig. 7 Locations of the four collapsed buildings and one damaged bridge relative to the Milun Fault



Fig. 8 **a** Front view, **b** back view, **c** drawing of floor plan, **d** corner column, and **e** and **f** bottom columns of the collapsed 12-story mixed-use apartment block

current code requirements (CICHE 2011). Figure 8f shows that the column moved upward and failed where splicing of reinforcements was deficient.

3.2 Collapsed 11-story hotel

The collapsed hotel was built forty years ago, i.e., in 1978. Figure 9a, b show the appearances of the hotel before and after this seismic event, respectively. Except for the colorful peripheral slender columns, the building essentially overhung the second and above floors (Fig. 9a). After the seismic event, because the bottom two stories were completely crushed, the building appeared as if the third floor was at ground level (Fig. 9b). Because the bottom

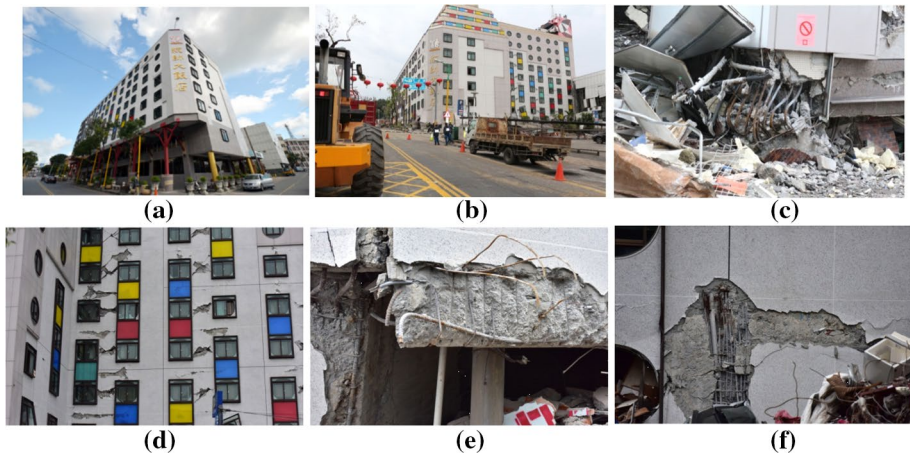


Fig. 9 Appearances of the hotel **a** before and **b** after the earthquake. **c** Crushed column, **d** shear cracks, **e** damaged beam, and **f** damaged beam of the collapsed hotel

story of this hotel had large open spaces used for reception, the number of RC walls of the bottom story were fewer than those of the other stories. Moreover, it was very possible that the seismic design and analysis of this aged building neglected the effects of partition walls, i.e., only the beam–column frame structure was considered. With this possible discrepancy between the actual building and the idealized analytical model, the presence of significantly different amounts of RC walls between the bottom story and the other stories very likely resulted in a soft-and-weak bottom story. In addition, without appropriate amounts of walls, the bottom columns probably sustained excessive axial loads during the earthquake. Figure 9c clearly shows that the columns' main reinforcements, which were confined with sparse stirrups, bulged outward, i.e., buckled. According to Fig. 9c, the spacing of the sparse stirrups appears to be greater than 30 cm. Because of the large width-to-height ratio of the building and because the bottom columns had deficient bearing capacities, the soft-and-weak bottom story eventually led to a “sit-down” type of collapse. In comparison, the collapsed 12-story mixed-use apartment (Fig. 8) had a smaller width-to-height ratio in the collapse direction (i.e., the south-west direction). In the light of Fig. 8c, the eventual collapsed form of the mixed-use apartment was a “knee-down” type (Fig. 8a). Perhaps, without the yellow steel struts (Fig. 8a), the mixed-use apartment might have been totally overturned during aftershocks. In such a case, the eventual collapsed form of the mixed-use apartment would be a “lie-down” type.

The numbers of casualties resulting from the three types of collapse, i.e., the sit-down, knee-down, and lie-down types, are different. Except for the crushed bottom story, the people residing in the other stories of sit-down collapsed buildings obviously have better chances of escaping with their lives. Compared with the sit-down type of collapse, people staying in partially crushed stories in addition to the upper stories of knee-down collapsed buildings may have chances of surviving. In the worst scenario, most residents of all the stories of lie-down collapsed buildings appear to have no chance of surviving. Therefore, when budgets for comprehensive seismic retrofitting of buildings are insufficient, even just altering the collapse type, e.g., from a lie-down type to sit-down or knee-down type, can substantially reduce the potential for severe casualties. The benefit-to-cost ratio of altering a building's collapse type appears to be significant. The counterpart in bridge engineering is the exploitation of simple devices to prevent bridge girders from unseating.

Figure 9d shows the inclined shear cracks of the exterior columns. Some of the shear cracks are cross-shaped, composed of two inclined cracks centered on one point. The column lengths shortened by windowsills (i.e., the deformations of columns restrained by windowsills) might be the main cause of the shear cracks occurring in the middle of the columns. Figure 9e indicates that the ends of the beams' bottom reinforcements were bent downward. In contrast, according to the latest suggestion of RC construction practice (CICHE 2011), the ends of the beams' bottom reinforcements should be bent upward into the connected columns to prevent damage to beam-to-column joints. Figure 9f depicts a damaged beam-to-column joint without sufficient numbers of stirrups in the joint.

3.3 Collapsed 9-story apartment building

Figure 10a, b show the front and back of the tilted 9-story apartment building, which was built in 1994. Figure 10c is a close-up photograph of the bottom story shown in Fig. 10a. The bottom story of this building was used as a parking lot. Figure 10c indicates that there were two spans (i.e., three columns) along the direction shown in the photograph. The front, middle, and back columns circled in yellow were all bent at their tops. In addition, all

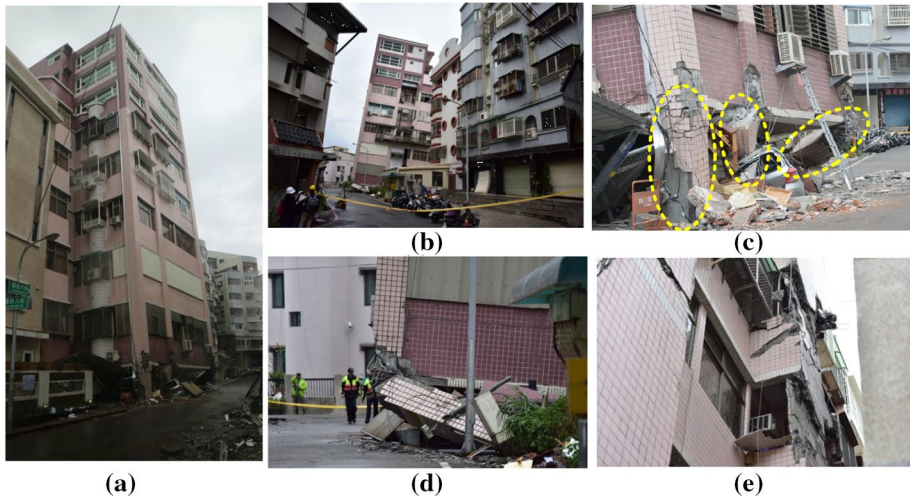


Fig. 10 **a** Front and **b** back views of the collapsed 9-story apartment building. **c** and **d** Close-up photographs of the bottom story shown in **a** and **b**, respectively. **e** Exterior walls of the collapsed building

three columns were inclined toward the inside of the building, and the inclinations sequentially increased from the front column to the back column (Fig. 10c). As a result, the extent of the damages at the tops of the three columns sequentially increased from the front to the back columns. In detail, the top of the front column remained joined to the upper column. In contrast, the top of the middle column was almost entirely separated from the above column. Additionally, the surface of the break at the top of the middle column appeared smooth and there appears to be almost no reinforcements going through that surface. The back column, which was the most severely damaged among the three columns, was almost laid down as a rigid block. The back column shown in Fig. 10c can also be seen from the rear side of the apartment building shown in Fig. 10b, d. Figure 10d is a close-up photograph of the bottom story shown in Fig. 10b. Figure 10d indicates that the back column remained essentially intact except that the column's top was broken. The reinforcements and stirrups at the top portion of the back column were insufficient (Fig. 10c). Additionally, the appearances of the 2nd-story columns atop the three 1st-story columns were all torn off at different lengths and this sequentially increased from the front column to the back column (Fig. 10c). From Fig. 10d, the ends of the reinforcements of the beam connected to the back column were bent downward. Similarly to the discussion associated with Fig. 9e, the bending direction for the ends of the bottom reinforcements of the beams is upward rather than downward. Figure 10e shows the broken exterior walls and the detachment of the exterior tiles of the 9-story apartment building. From the broken section of the exterior walls, there seem to have been very few reinforcements in the exterior walls.

In light of the above-mentioned substantially unequal inclinations and damage extents of the three bottom columns shown in Fig. 10c, the frame consisting of these three columns very likely underwent rotation-induced out-of-plan displacements. In other words, the apartment building was probably plan-asymmetric, which had stiff and flexible sides at the front and back columns of Fig. 10c, respectively. In addition, according to the situations of the reinforcements and concretes exposed at the tops of the bottom columns,

the construction appears to have been poor and perhaps was not built following the design drawings. Furthermore, it is worth noting that the color of the exterior tiles on the top three stories was obviously darker than those on the below six stories (Fig. 10a, b). According to statements from the residents of the building, the top three stories were added later, i.e., the original building was a six-story building. Whether or not the added top three stories were legal may require investigation by authorities. If the added top three stories were illegal, then the original six-story building would very likely not have had sufficient capacity to sustain the additional weight and lateral inertial force induced by the added three stories during an earthquake.

3.4 Collapsed 6-story apartment building

Figure 11a shows the collapsed 6-story apartment building, which was within an approximately 1-min walking distance from the aforementioned 9-story building (Figs. 7 and 10). The collapsed 6-story apartment building was constructed in 1992. Unlike the 9-story building (Fig. 10), which had a knee-down collapse, the bottom story of this 6-story apartment building (Fig. 11a) was also used as a parking lot and it displayed a sit-down collapse. This implies that the bottom-story parking lots with their open spaces and fewer partition walls caused soft bottom stories and this led to the collapse of the building. Furthermore, the possible translation–rotation coupled displacements of the 9-story building (Fig. 10) resulted in a knee-down collapse, such that the damages to the columns were unevenly distributed (Fig. 10c). In contrast, the sit-down collapse of the 6-story building (Fig. 11a) implies that the displacement demands of its bottom columns were approximately equal, i.e., only translational displacements occurred.

The central part of Fig. 11a (the exterior walls of the balconies of all stories) are magnified in Fig. 11b for clarity. These exterior walls have similar patterns of cracks, as indicated

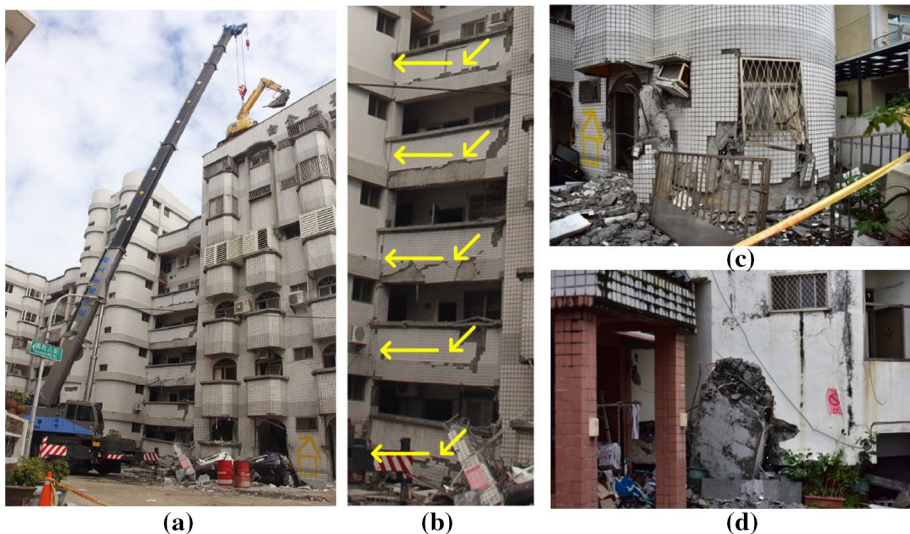


Fig. 11 **a** Front view of the collapsed 6-story apartment building and **b** a magnification of the central part of **a**. **c** Front and **d** back close-up photographs of the collapsed building

by the yellow arrows shown in Fig. 11b. In detail, each of these cracks started at the top right corner of the exterior wall of the balcony and then propagated left and downward with an approximate 45° inclination. Once the crack touched the top surface of the slab of the balcony, it propagated continuously and horizontally to the left side of the balcony. This pattern of cracks implies that the shear force was transferred at the right sides of the balconies. Additionally, there were weak junction surfaces between the slabs and the walls of the balconies. Figure 11c, d show the front and back walls of the apartment building on the ground. While the building settled, there should be substantial vertical reaction forces. The iron-grated window shown in Fig. 11c, which was a weak region of the wall, was extruded outward. The form of the flaked concrete extending out of the wall shown in Fig. 11d was similar to that of the window shown in Fig. 11c. This might reflect that the flaked concrete was a weak region of the back wall. Therefore, it is unsurprising to find that the quality of the concrete exposed at this weak region was poor (Fig. 11d).

A few days after the earthquake, a crane lifted an excavator equipped with a drill bit to the roof of the collapsed apartment building to start demolition work (Fig. 11a). It is worth noting that demolition of the nearby collapsed 9-story building (Fig. 10) was performed after demolition of this 6-story building (Fig. 11). This is because the engineers responsible for the demolition of these two buildings wanted to use the debris of the demolished 6-story building to wedge up the tilted 9-story building. The purpose of wedging the 9-story building was to prevent other surrounding buildings from being damaged by a possible lie-down collapse of the 9-story building during demolition.

Buildings where the first stories are elevated as lobbies, shopping stores or parking lots and where the other stories are used as residences are very common in Taiwan. Nevertheless, many such buildings with the conditions (e.g., location, age, number of story) similar to those of the four collapsed buildings (Figs. 8, 9, 10, 11) satisfactorily sustained the strike of the Hualien earthquake. It is highly likely that multiple factors led to the collapses of the four buildings. Besides the possible design/construction deficiencies, the spectral accelerations surpassing the design response spectrum at medium to long periods (Fig. 5b) caused by near-fault effects certainly related to the collapses of the four buildings.

3.5 Damaged 12-story department store

The damaged 12-story department store (Fig. 12a) was opened in 1991. After being damaged during the 1999 Chi-Chi earthquake, the department store was once repaired and retrofitted. The department store was moved to another building in 2009. Hence, the building was abandoned and empty when the 2018 Hualien earthquake occurred. The staircases at the back of the building were retrofitted with steel braced frames after the 1999 Chi-Chi earthquake (Fig. 12b). The staircases and the added steel braced frames remained essentially intact after the 2018 Hualien earthquake. In contrast, a brick wall appearing at the right bottom corner of Fig. 12b was cracked. This might imply that the added steel braced frames performed well such that the building was protected to some extent. Figure 12c shows that the lateral walls of the building were damaged with diagonal shear cracks. Moreover, the exterior columns of the bottom story shown in Fig. 12d, e were severely damaged with a deep and wide shear crack and a flexure-shear crack, respectively. The spacing of the stirrups shown in Fig. 12e was extraordinarily large, which was approximate 25 cm. Additionally, most of the decorated white stone panels encasing the columns had flaked off (Fig. 12d, e). The severely damaged building (Fig. 12) was eventually demolished after the Hualien earthquake.

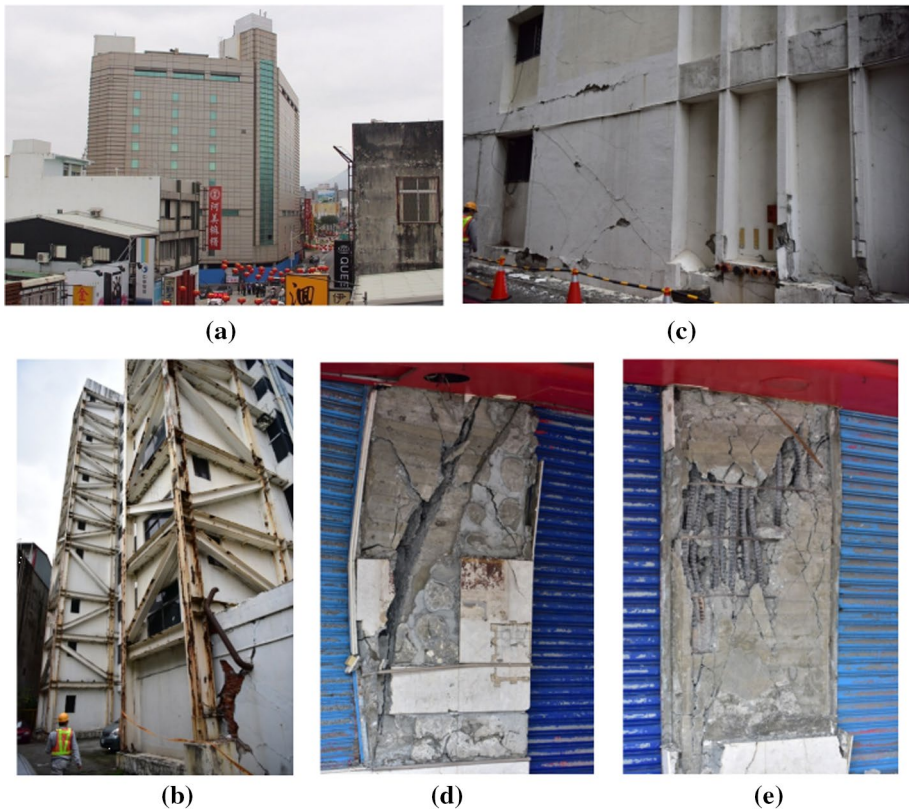


Fig. 12 Photographs of the damaged 12-story department store: **a** overall view, **b** retrofitting with a steel braced frame, **c** side view, and **d** and **e** severely damaged bottom columns

3.6 Base-isolated building

The base-isolated building is a regional hospital with ten floors and two base floors (Fig. 13a) located approximately 2 km away from the Milun Fault. The second base floor, abbreviated as B2F, is dedicated to installation of the isolators, which are lead rubber bearings (LRB) (Fig. 13b). There were no structural damages found in the building as a whole, including the isolators and the upper structure. Nevertheless, damages to some non-structural components were observed (Fig. 13c–f). Figure 13c shows the broken glass that was used for protecting and encasing the displayed seismic instruments. The reserved gap allowing lateral deformations of LRBs is 70 cm. The planks covering the reserved gap were inclined and pushed aside, leaving a space between the planks and the pavements of walkways (Fig. 13d). Some other segments of the reserved gap were covered using checker plates (Fig. 13e), which were damaged and disordered. Additionally, Fig. 13f shows damaged piping supports. Besides the seriously deformed piping support indicated on the left of Fig. 13f, the end of the right piping support was detached from the pipe (Fig. 13f). Although these non-structural damages did not affect the operation of the hospital, it shows that more attention to the details of non-structural components of buildings with seismic isolators is needed in comparison with conventional buildings.

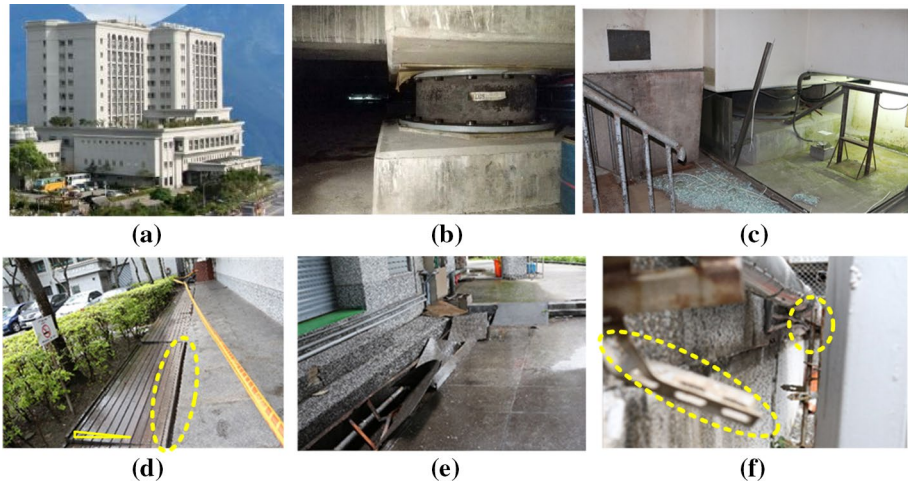


Fig. 13 Photographs of **a** the base-isolated building, **b** a lead rubber bearing, **c** broken glass, **d** gaps induced by the deformation of isolators, **e** damaged checker plates, and **f** damaged piping supports

The base-isolated building (Fig. 13a) has been monitored with seismic instruments since the opening of the hospital. Figure 14 shows the layouts of the seismic instruments, including twenty-six channels for accelerators and four channels for displacement transducers. The four channels for displacement transducers are numbered CH27 to CH30 in Fig. 14b. The other numbered channels shown in Fig. 14 are for accelerators. Figure 15a–c show the acceleration histories in longitudinal, transverse, and vertical directions, respectively, recorded on the B2F level. In addition, the records obtained from the accelerometer located at the center of B2F (i.e., CH1 to CH3) are compared with those obtained from the accelerometer located at the corner of B2F (i.e., CH4 to CH6). Figure 15d–f are the counterparts of Fig. 15a–c for the roof’s acceleration records. The consistency between the acceleration histories recorded at the centers and corners of the floor plans (Fig. 15) indicates that there were no rotational responses, i.e., there were pure translations in both horizontal directions. These observed pure translations might have two meanings. One is that the building is symmetrical, i.e., it has no plane eccentricities. The other is that the accidental torsion stipulated in modern building codes (e.g., ASCE 2010; Eurocode-8 2003; CPAMI 2011)

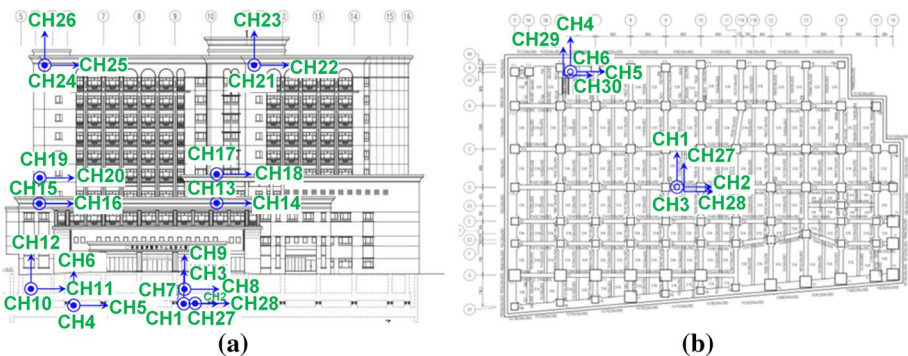


Fig. 14 Layouts of seismic instruments in **a** elevation and **b** floor plan of B2F

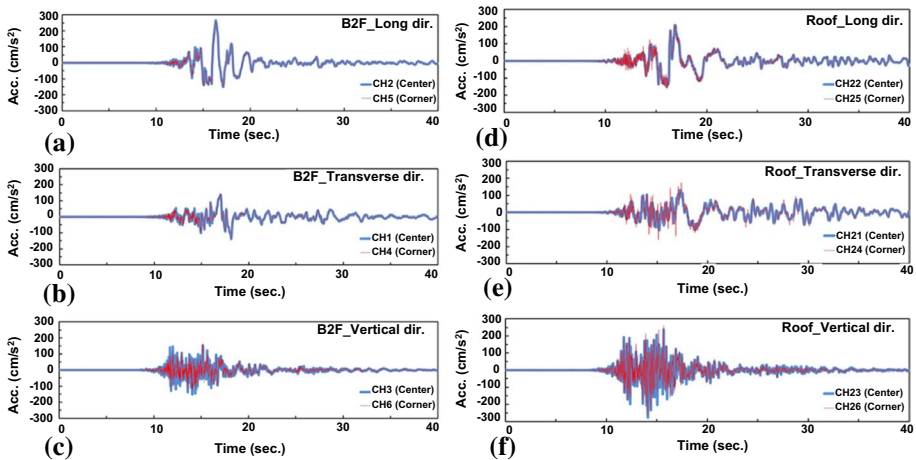


Fig. 15 Acceleration histories recorded at B2F in the **a** longitudinal, **b** transverse, and **c** vertical directions, and recorded at the roof in the **a** longitudinal, **b** transverse, and **c** vertical directions

were not notably reflected in this building under the shaking of the earthquake. It is clear that the code-specified accidental torsion reflects the effects of the possible rotational components of ground motions, and the possible discrepancies between the actual and designed distributions of mass, stiffness and yielding strength of structural members. Therefore, the code-specified accidental torsion is a conservative design requirement, at least for this building under the shaking of the Hualien earthquake.

Figure 15 also shows that the values of the longitudinal, transverse, and vertical peak accelerations are 209, 131, and 279 cm/s^2 , respectively, at the roof's center (Fig. 15d–f), and 266, 139, and 155 cm/s^2 , respectively, at the center of B2F (Fig. 15a–c). Therefore, the ratios of the longitudinal, transverse, and vertical peak accelerations recorded at the roof's center to those recorded at the center of B2F are 0.79, 0.94, and 1.8, respectively. In other words, the percentages of the reduced accelerations in the longitudinal and transverse directions were 21% and 6%, respectively, whereas the acceleration in the vertical direction increased by 80%. The acceleration response spectra corresponding to the ground motion records of strong motion station HWA019 (Fig. 5b) indicate large acceleration demands for structures with vibration periods of 2 to 4 s. Because both the designed first vibration periods in the longitudinal and transverse directions of this building (Fig. 13a) are 2.76 s, it is expected that the effect of the base isolation used in this building on reducing the peak accelerations was not significant in this seismic event. This unremarkable seismic performance of the base isolation indicates that the effect of near-fault ground motions on base-isolated buildings should be properly and thoughtfully considered. Moreover, it is clear that LRBs isolate horizontal ground accelerations rather than vertical ground accelerations. Therefore, considering that the vertical vibration period is very short, the 80% increment of the peak vertical acceleration of the roof in comparison with that of B2F appears reasonable.



Fig. 16 **a** and **b** Cracked brick walls. **c** A cracked column of a four-story school building

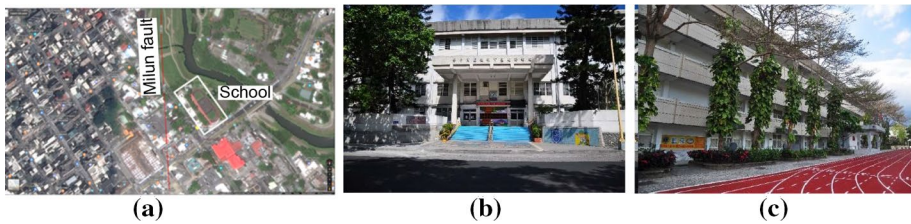


Fig. 17 **a** Map showing a school close to the Milun Fault. **b** Central front and **c** overall views of the school building

3.7 School buildings

With the authorization of Taiwan's Ministry of Education, the NCREE has performed seismic evaluation and retrofitting of school buildings across Taiwan since 2009 (Hwang et al. 2012). Until the end of 2017, the seismic resistances of 92% of school buildings nationwide were secure. By the end of 2017, twenty-four out of the total 876 school buildings of Hualien County still needed to be retrofitted (Jiang et al. 2018). Fortunately, these twenty-four school buildings in line for retrofitting had no structural damages during the Hualien earthquake. Moreover, most observed seismic damages to school buildings caused by the Hualien earthquake were facility damages, e.g., overturned bookcases and computer monitors, leakages of water pipes, and fallen ceilings. Only two retrofitted school buildings of Hualien County had minor structural damages, which were acceptable to the project of seismic evaluation and retrofitting of school buildings. The minor structural damages of the two school buildings are described as follows.

Figure 16a, b show the cracks in brick walls surrounding the lavatories of a four-story school building that was retrofitted with steel braces and had shear walls added in 2010. Figure 16c shows the cracks induced by pounding between a column and a sink in the other school building. The cracked column and the basin were from one two-story building and one four-story building, respectively. The two- and four-story buildings, which were built in 1984 and 1997, respectively, were arranged in an L-shape and separated with expansion joints. The basin was added to the second floor of the four-story building during the seismic retrofit conducted in 2014. However, there were no reserved gaps between the sink and the column. Because of the different vibration periods of the two buildings, the collision between the sink and the column during ground shakings was inevitable.

Figure 17a shows an elementary school close to the Milun Fault. The school has only one building, which has four stories and one basement floor constructed in 1990. This school building was retrofitted with enlarged columns, added shear walls, and wing walls

in 2011. Even though this school building is close to the Milun Fault, no structural damages were found in the building (Fig. 17b, c). Moreover, it is worth mentioning that two retrofitted buildings of a junior high school were intact during the 2016 Meinong earthquake. In contrast, two other buildings of the same school that had not been retrofitted at the time of the 2016 Meinong earthquake suffered obvious damages in that seismic event (Henry et al. 2017; Shen et al. 2016). Therefore, in addition to the aforementioned case of the 2016 Meinong earthquake, the results of the reconnaissance demonstrate again that the project of seismic evaluation and retrofitting of school buildings across Taiwan initiated in 2009 was quite successful.

3.8 Non-structural components

Besides damages to building structures, the damages to non-structural components of buildings are also discussed. Figure 18a–c show the different extents of damage to shelves of medical history sheets in a hospital. The shelves shown in Fig. 18a, b were identical and were moveable on their own wheels. Nevertheless, the countermeasures adopted for resisting seismic forces on the shelves were different. The shelves of Fig. 18a were fixed to the floor slabs via angle steels connecting the shelves' bottoms and the floor slabs with bolts. In contrast, the shelves of Fig. 18b were connected to each other via the links at the shelves' tops. Because of the insufficiency of the bolts connecting the shelves' bottoms and the floor slabs, the shelves in Fig. 18a were overturned. In contrast, because the added top links substantially increased the width-to-height ratio of the shelves, the only damage to the shelves in Fig. 18b was warped sideboards. The shelves shown in Fig. 18c were of another type that was moveable on sliding rails mounted on the floor slabs. Only some sideboards of the shelves shown in Fig. 18c were slightly inclined. It was also noted that the normal



Fig. 18 a–c Damaged shelves for medical history sheets in a hospital. **d** An overturned medicine refrigerator. **e** Fallen ceilings in a hospital. **f** Books fallen from bookshelves. Overturned **g** filing cabinets and **h** desk computers. **i** A damaged water storage tank

vectors of the vertical planes of the shelves shown in Fig. 18a, b were in a NE-SW direction that was almost in line with the direction of most of the velocity pulses observed in the Hualien earthquake (Fig. 3). In other words, the velocity pulses were essentially along the short direction of the shelves shown in Fig. 18a, b. In contrast, the direction of the shelves shown in Fig. 18c was 90° rotated relative to the shelves shown in Fig. 18a, b. In other words, the velocity pulses were essentially along the long direction of the shelves shown in Fig. 18c. In addition, in light of the reserved large spacing between the shelves (Fig. 18a), a domino effect might be one of the reasons causing the overturning of a series of shelves, as shown in Fig. 18a. In contrast, the close spacing between the shelves shown in Fig. 18c might prevent the occurrence of a domino effect.

The other damages to non-structural components commonly observed in hospital buildings were the overturning of medicine refrigerators (Fig. 18d) and the fall of ceilings (Fig. 18e). The fallen ceilings shown in Fig. 18e were in front of the doors of elevators and the entrance to stairs. It is worth noting that no matter what the categories of the buildings (hospital, school, etc.), most of the falls of suspended ceilings occurred at the peripheral parts of the ceilings. This implies that possible collision between the suspended ceiling and its surrounding structural members (e.g., beams, walls) should be one of the main concerns of the seismic design of such ceilings.

Typical non-structural damages to schools during this seismic event were books falling from bookshelves (Fig. 18f), the overturning of filing cabinets and desk computers (Fig. 18g, h), and damaged water storage tanks (Fig. 18i). Figure 18i shows that the supporting frame of an overturned water storage tank was significantly deformed. This type of water storage tank, made of aluminum, is commonly installed on the roofs of buildings across Taiwan. Nevertheless, their supporting frames seem not to be differentiated for the different heights of buildings. In other words, the supporting frames are sold as accessories to the sets of water storage tanks rather than customized products. Therefore, it appears necessary to establish rational commercial codes or standards for such water storage tanks.

In addition to hospitals and schools, a terminal of an airport (Fig. 19) located approximately 1 km away from the Milun Fault was also examined after the earthquake. This terminal had three floors and one basement floor and was constructed in 2004. The baffle boards (Fig. 19a) and the ceilings, made of punched aluminum plates (Fig. 19b), had fallen during the earthquake, even though the terminal was relatively new. Figure 19c shows a ventilation duct hanging through the hole where the ceilings fell. The damaged sprinkler pipe for firefighting (Fig. 19d) resulted in the leakage of water in the arrival hall.

Although no people were hurt by these non-structural damages during the seismic event, the seismic damages illustrated in Figs. 18 and 19 caused impaired functionalities, economic losses, and slowed restoration works.



Fig. 19 **a** Fallen baffle boards, **b** fallen metal ceilings, **c** a ventilation duct hanging through the hole where the ceilings fell, and **d** a damaged sprinkler pipe used for fire-fighting in an airport terminal

Except designed spectral accelerations varying from seismic zone to seismic zone, the building designs in all regions of Taiwan are essentially the same. Because damaging earthquakes have frequently occurred in Taiwan, collapsed buildings were not rare in the past seismic events of Taiwan. Figure 20a, b illustrate collapsed buildings during the 1999 Chi-Chi earthquake and the 2016 Meinong earthquake, respectively. Figure 20c is a bird's eye view of the same building shown in Fig. 20b. Both the lie-down collapsed buildings (Fig. 20a, b) resulted in drastic fatalities. Additionally, Fig. 20d shows a knee-down collapsed building during the 2016 Meinong earthquake. The damage patterns of the three collapsed buildings (Fig. 20a, b, d) are similar to those of the four collapsed buildings observed in the Hualien earthquake (Figs. 8, 9, 10, 11), i.e., collapse mechanisms formed at the bottom stories. Unevenly distributed deformations resulting from structural plan asymmetry also existed in some of the buildings collapsed during the present earthquake (e.g., Figs. 8 and 10) and the past earthquake (e.g., Fig. 20d). Moreover, the construction years of the two collapsed buildings shown in Fig. 20b, d are 1994 and 1992, respectively, which are similar to those of the collapsed buildings in the Hualien earthquake except the collapsed 11-story hotel (Fig. 9). In comparison with the 2016 Meinong earthquake, the observed velocity pulses of the Hualien earthquake were much more intense. All the four collapsed buildings in the Hualien earthquake were near fault (Fig. 7), which is a particular phenomenon compared with the past seismic events of Taiwan.

4 Bridges

Soon after the Hualien earthquake, passage over four bridges, namely the Qixingtian Bridge, Hualien Bridge, Hualien City No. 3 Bridge, and Shangzhi Bridge, were temporarily blocked for safety inspections. The Qixingtian Bridge and Hualien Bridge cross the northern parts of the Milun Fault and the Lingding Fault, respectively (Fig. 21a). Figure 21b, c illustrate the directions of the Qixingtian and Hualien Bridges relative to the Milun and Lingding Faults. The two bridges are shown as blue strips in Fig. 21b, c, in which the abutments are denoted as A1 and A2. The strong ground motion stations HWA028 and HWA060 are close to Qixingtian Bridge and Hualien Bridge, respectively (Fig. 21a). Both the PGAs recorded at HWA028 and HWA060 were over 400 cm/s^2 (Table 1), which is Taiwan's strongest seismic intensity level VII. The reconnaissance results for Qixingtian Bridge and Hualien Bridge are as follows (Hung et al. 2018).

Figure 21d, e respectively show the horizontal and vertical displacements of land surfaces measured through the global positioning system (GPS) by Taiwan's



Fig. 20 **a** A 12-story building collapsed during the 1999 Chi-Chi earthquake, **b** a 16-story building collapsed during the 2016 Meinong earthquake, **c** a bird's eye view of the collapsed building shown in **b**, **d** a 7-story building collapsed during the 2016 Meinong earthquake

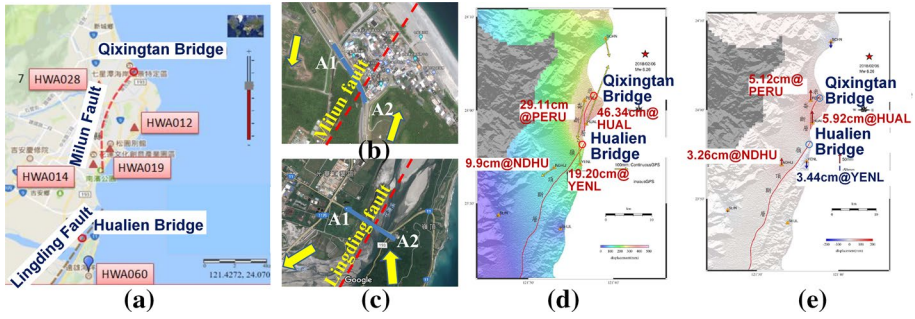


Fig. 21 a Locations of the Qixingtian Bridge and Hualien Bridge. b The direction of Qixingtian Bridge relative to the Milun Fault. c The direction of the Hualien Bridge relative to Lingding Fault. The d horizontal and e vertical displacements of land surfaces on the two sides of the Milun Fault and Lingding Fault (CGS 2018)

Central Geological Survey (CGS 2018). The lengths and directions of the arrows shown in Fig. 21d, e represent the magnitudes and directions of the displacements. The GPS monitoring stations HUAL and PERU are on the hanging wall (or east side) and footwall (or west side) of the Milun Fault, respectively. The horizontal displacements at the HUAL and PERU stations were 46.34 cm toward the north-east direction and 29.11 cm toward the south-west direction, respectively (Fig. 21d). That is to say, the relative horizontal displacement between the hanging wall and the footwall of the Milun Fault, dislocated in the Hualien earthquake, was over 70 cm. Additionally, the vertical displacements at the HUAL and PERU stations were 5.92 cm and 5.12 cm, respectively, both of which were upward (Fig. 21e). Moreover, the GPS monitoring stations YENL and NDHU are on the hanging wall (or east side) and footwall (or west side) of Lingding Fault, respectively. The horizontal displacements at the YENL and NDHU stations were 19.2 cm toward the north-west direction and 9.9 cm toward the south-west direction, respectively (Fig. 21d). The vertical displacements at the YENL and NDHU stations were downward 3.44 cm and upward 3.26 cm, respectively (Fig. 21e). The directions of the yellow arrows shown in Fig. 21b, c are the same as those of the arrows shown in Fig. 21d. Figure 21b, c clearly indicate that the overall land displacements of Qixingtian Bridge and Hualien Bridge were counterclockwise. Differential land displacements indeed existed in each of the bridges. In addition, the major land displacements of Qixingtian Bridge and Hualien Bridge were on the hanging wall (or east side), i.e., on the abutment A2 side.

4.1 Qixingtian bridge

Figure 22a depicts a plan and elevation layouts of Qixingtian Bridge, which was opened for traffic in 2013. Abutment A1 to pier P1 is a 60-m-span simply supported vibration unit where the bearing at abutment A1 is longitudinally moveable and the bearing at pier P1 is a hinge. Pier P1 to abutment A2 is another vibration unit that is a two-span, 90 m + 90 m, continuous girder rigidly connected to pier P2 (Fig. 22a). In this two-span vibration unit, both the bearings at pier P1 and abutment A2 are moveable in the longitudinal direction and fixed in the transverse direction, and vertically adjustable. Abutment A2 is skewed relative to the direction of traffic flow. The superstructure of the bridge consists of

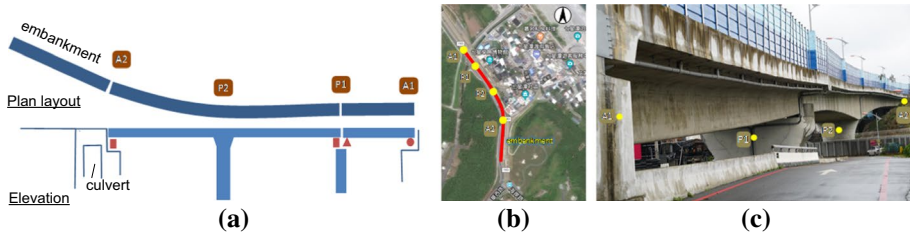


Fig. 22 Qixingtan Bridge: **a** diagrams of the plan and elevation layouts, **b** satellite image, and **c** photograph

pre-stressed concrete two-cell box girders. The substructure of the bridge is single-column RC piers with elliptical cross-sections and pile foundations. In addition, there is a culvert integrated with abutment A2 (Fig. 22a). Figure 22b, c show respectively a satellite image and a photograph of the Qixingtan Bridge. The serial numbers of the piers and abutments are marked in the photographs (Fig. 22b, c).

Figure 23a, b show the upheaval of the road embankment approaching abutment A2. In light of the displacements of the land surface shown in Fig. 21b, d, there was a thrust from the embankment toward abutment A2, by which the aforementioned upheaval was manifested. Additionally, that is why the noise barriers at the top of the upper-left corner of the culvert were pushed against each other (Fig. 23c). Figure 23d shows the cracked seismic stopper at abutment A2. This slightly damaged seismic stopper implies an inclined rather than perpendicular collision between the girder and the seismic stopper because abutment A2 is skewed relative to the direction of traffic flow. Pier P2 was intact (Fig. 23e), whereas pier P1 had obvious damage (Fig. 23f, g) caused by the collision between the girder and the seismic stopper. This collision also resulted in the surrounding concrete flaking off pier P1. Nevertheless, through detailed visual inspection, there were no visible flexural or shear cracks at the bottom of pier P1. The damage to the seismic stoppers (Fig. 23d, f, and g) reflects that the seismic stoppers functioned properly. Figure 23h shows the essentially intact expansion joint at abutment A1. Nevertheless, it is noted that the red traffic markings on the opposite sides of the expansion joint were not in line with each other (Fig. 23h).

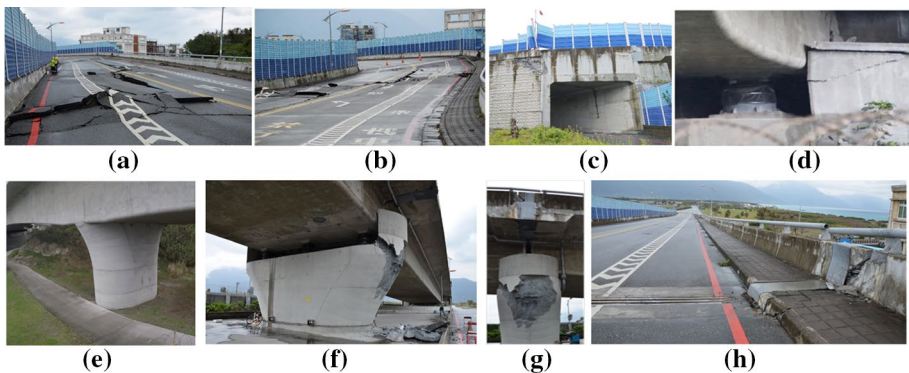


Fig. 23 **a** and **b** Upheavals of the road embankment approaching abutment A2. **c** The damaged noise barriers above the culvert. **d** The cracked seismic stopper at abutment A2. **e** The intact pier P2. **f** and **g** The damaged pier P1. **h** The expansion joint of abutment A1

This indicates that different transverse displacements occurred on the two sides of abutment A1. Considering the large dislocation of the Milun Fault and the structural integrities of piers P1 and P2 (Fig. 23e, f), Qixingtian Bridge performed well in this seismic event.

4.2 Hualien bridge

Figure 24a depicts top and side views of the Hualien Bridge, whose structures for the northbound and southbound routes are completely separated. The southbound and northbound routes, completed in 1968 and 2002, respectively, are designated as 1st- and 2nd-generation bridges (Fig. 24a). Both the 1st- and 2nd-generation bridges were seismically retrofitted in 2013. Figure 24b, c show the satellite image and a photograph of the Hualien Bridge, respectively. Figure 24a indicates the span layouts and the bridge widths. Each span of the 1st-generation bridge consists of simply supported pre-stressed I-shaped girders sitting on neoprene pads. Expansion joints are set between every two spans of the bridge. The substructure of the 1st-generation bridge consists of circular single-column piers supported by circular caissons. Additionally, the foundations of piers P5 to P12 were retrofitted with extended pile caps and added piles in 2013 (Fig. 24a). The layout of the 2nd-generation bridge is similar to that of the 1st-generation bridge except that the former has no caissons but only piles. Besides abutments A1 and A2, the expansion joints of the 2nd-generation bridge are installed only at piers P3, P6, P9, P12, and P13 (Fig. 24a). The hinge-connected bridge decks are above the other piers where expansion joints are not installed. The 2nd-generation bridge was retrofitted with enlarged RC piers and added piles in 2013.

The bridge decks between the expansion joints at piers P9 and P12 were severely damaged. The directions of the yellow arrows in Fig. 25a indicate that the end of the expansion joint at pier P9 of the 2nd-generation bridge (on the side near the 1st-generation bridge) was opened, whereas the other end of the expansion joint was closed. Likewise, the end of the expansion joint at pier P9 of the 1st-generation bridge (on the side near the 2nd-generation bridge) was closed, whereas the other end of the expansion joint was opened. For clarity, Fig. 25b, c, which are magnifications of Fig. 25a, show the expansion joints at pier P9 of the 1st- and 2nd-generation bridges, respectively. From Fig. 21c, the northbound and southbound routes can be viewed as two parallel beams being bent with their tops compressed (i.e., suggesting closed expansion joints) and bottoms tensioned (i.e., suggesting opened expansion joints). Therefore, the non-uniform movements of the expansion joints (Fig. 25a) are consistent with the displacements of the land surface near the Hualien Bridge (Fig. 21c). The deflected white traffic markings between piers P9 and P10 (Fig. 25d) indicate that pier P10 moved northward relative to pier P9, which also reflected

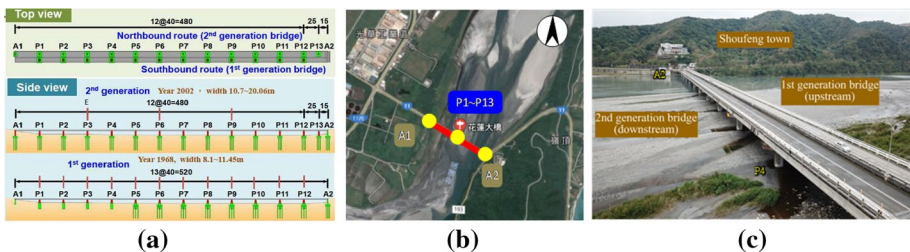


Fig. 24 a Top and side views, b satellite image, and c photograph of Hualien Bridge

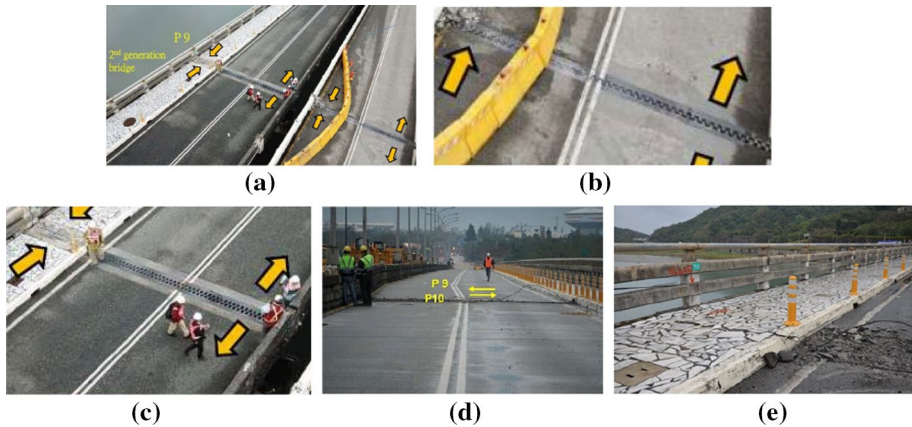


Fig. 25 **a** Expansion joints at pier P9. **b, c** Magnifications of **a**. **d** Deflected white traffic markings between piers P9 and P10. **e** Shattered bridge deck at pier P10

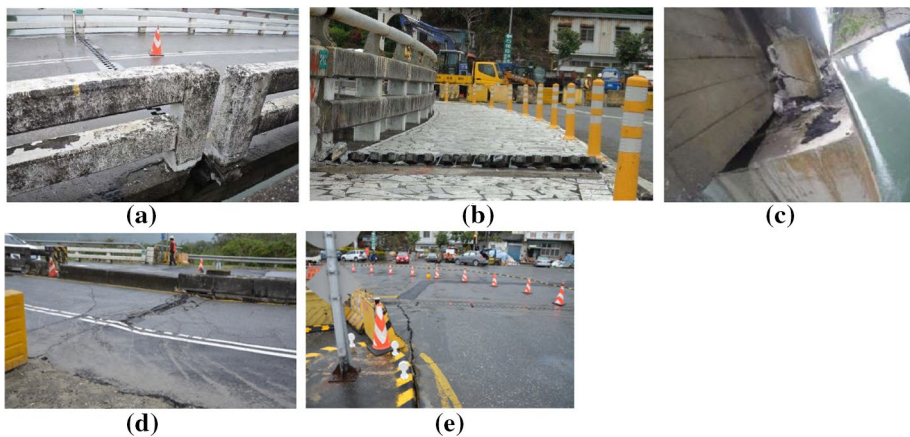


Fig. 26 **a** Southbound route at pier P12. **b** Northbound route at pier P12. **c** Cracked seismic stopper at pier P12. **d** Upheaval of road surface near abutment A1. **e** Cracked road surface near abutment A2

the displacements of the land surface near the Hualien Bridge (Fig. 21c). Figure 25e shows the shattered bridge deck at pier P10.

At the barriers at pier P12 of the southbound route (Fig. 26a), an approximately 15-cm transverse dislocation was observed. Additionally, the teeth of the expansion joint at pier P12 of the northbound route were not only transversely dislocated but also pushed upward (Fig. 26b). Because of the aforementioned transverse dislocation, collision between the girder and the seismic stopper resulted in the crack of the seismic stopper at pier P12 (Fig. 26c). The road surfaces near both abutments A1 and A2 were uplifted and cracked (Fig. 26d, e). This might have been caused by the pushing force of the approach slab of the bridge.

Differential displacements indeed occurred in the Qixingtian and Hualien Bridges, both of which cross active faults. This phenomenon implies that sufficient displacement capacity

is necessary for bridges crossing active faults. For bridges with simply supported girders sitting on neoprene pads or moveable bearings, the large displacement demands caused by the dislocations of active faults may be totally or partially accommodated by the girders' displacements relative to their bearings. The inertial forces transmitted to the substructures are thus reduced. Most of the seismic damages to such bridges likely occur at the bridge decks, expansion joints, and seismic stoppers. Certainly, the most critical challenge is to ensure that the displacement capacities of such bridges are sufficient for preventing the girders from unseating.

5 Liquefaction at Hualien port

Significant liquefaction was observed at Hualien Port. Figure 27a shows the location of Hualien Port relative to the Milun Fault. Hualien Port consists of inner and outer harbors with 25 deep-water wharfs. Wharfs No. 1 to No. 16 and wharfs No. 17 to No. 25 are located in the inner and outer harbors, respectively. The outer harbor was completed in the final stage of an expansion project in 1991. The major liquefaction occurred at wharfs No. 23 to No. 25 as well as the western breakwater. Figure 27b, magnified from Fig. 27a, shows the locations of wharfs No. 17 to No. 25. Because the direction of wharf No. 25 is approximately 135° clockwise from the direction of wharf No. 24 (Fig. 27b), there is a transition wharf at the turning corner, i.e., between wharfs No. 24 and No. 25. Figure 27c, d show the cross sections of the gravity-type caissons of wharfs Nos. 23 and 24 and wharf No. 25, respectively. The back areas of the caissons shown in Fig. 27c, d were backfilled with gravels and sands.

The settlement of back area of wharf No. 23 was approximately 200 mm (Fig. 28a). Besides sands accumulated at some points of wharf No. 23, the border between the caissons and the back area was cracked (Fig. 28a). Nevertheless, the caissons of wharf No. 23 were not damaged, displaced, or settled. Figure 28b, c are images from closed-circuit television (CCTV) installed at wharf No. 23 with recording times at respectively 23:50:51 and 23:51:16 on February 6, 2018. The two recording times, separated by only 25 s, are before and after the strong shaking of the Hualien earthquake. Comparing the two images shows the spurt of underground water and cracks in the pavements caused by the ground shaking. With the CCTV images, the accumulated sands, settlements, and cracks collectively indicate that soil liquefaction happened in this area. The damages to wharf No. 24 shown in Fig. 28d, e were similar to those of wharf No. 23, but the settlement of its back area, which was approximately equal to 200–300 mm (Fig. 28d), was more significant in comparison with that of wharf No. 23. In addition, there was an approximately 90 mm gap between the wave chambers of wharf No. 24 (Fig. 28f) near the turning corner of the wharf, i.e., the side close to wharf No. 25 (Fig. 27b).

Wharf No. 25 suffered more damage than wharfs No. 23 and No. 24 in this seismic event. A differential settlement appeared on the two sides of wharf No. 25 (Fig. 29a). This earthquake also induced a gap of 80–130 mm between wharf No. 25 and the transition wharf at the turning corner (Fig. 29b). The back area of wharf No. 25 settled to a depth of 500 mm to 600 mm (Fig. 29c). This was the largest settlement among all the wharfs of Hualien Port. Figure 29d–f show images of the western breakwater. Before the Hualien earthquake, parts of the roads on the western breakwater were maintained by repaving roads with rigid pavements instead of the original flexible pavements (Fig. 29d). After the

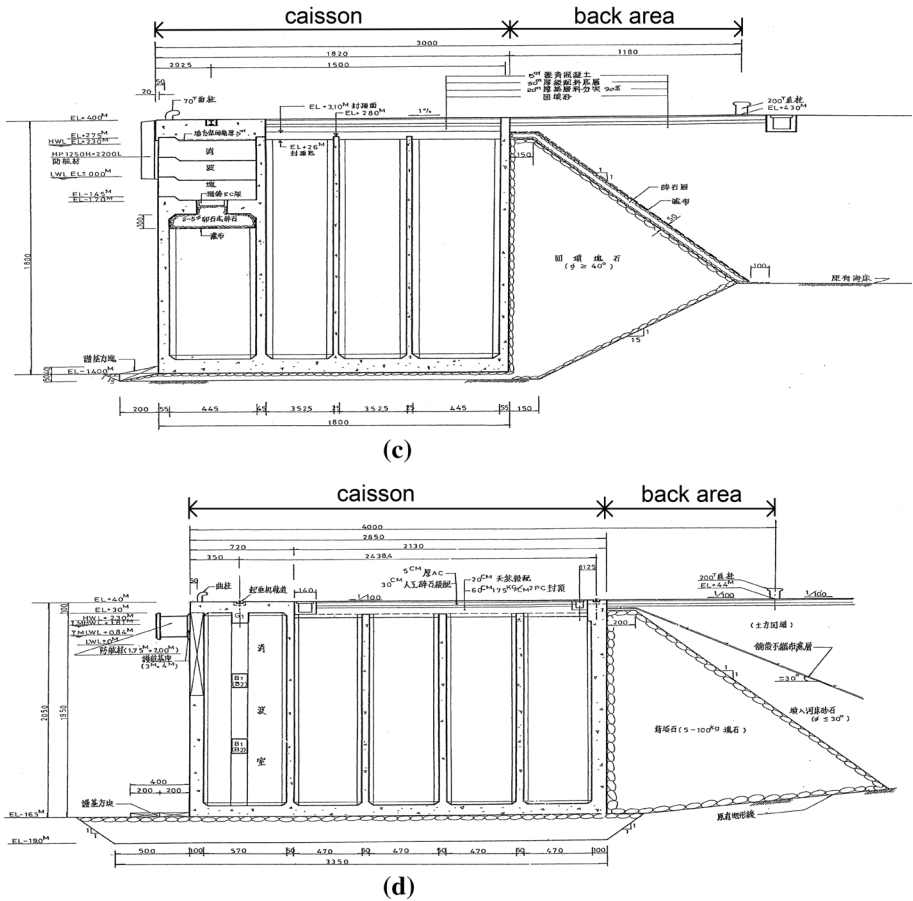


Fig. 27 Hualien port: **a** satellite image, **b** magnification of **a**, **c** cross-section of wharves No. 23 and No. 24, and **d** cross-section of wharf No. 25

Hualien earthquake, settlements and cracks occurred in the flexible pavements but not in the rigid pavements. A possible reason for this phenomenon is that the rigid pavements were capable of resisting the settlements induced by hollowing out of the roadbeds, where many sand vents were observed underneath the rigid pavements (Fig. 29e). Figure 29f

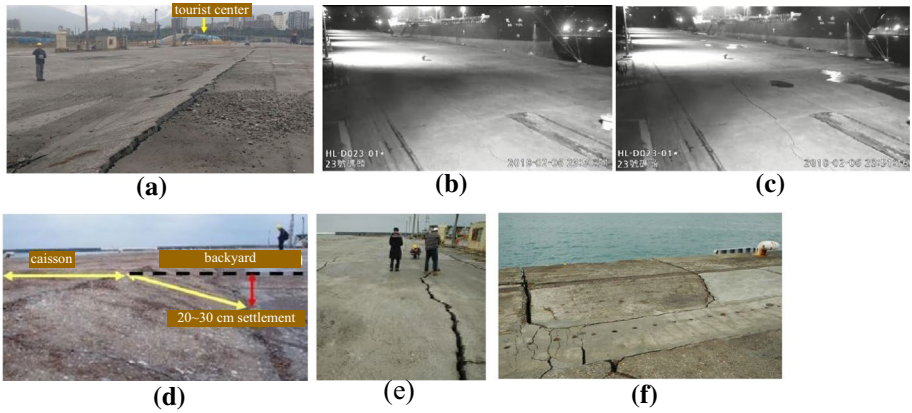


Fig. 28 a Accumulated sands and the settlement of the back area of wharf No. 23. CCTV images of wharf No. 23 (b) before and (c) after the strong ground shaking. d The settlement and e the crack of the back area of wharf No. 24. f The gap between wave chambers of wharf No. 24

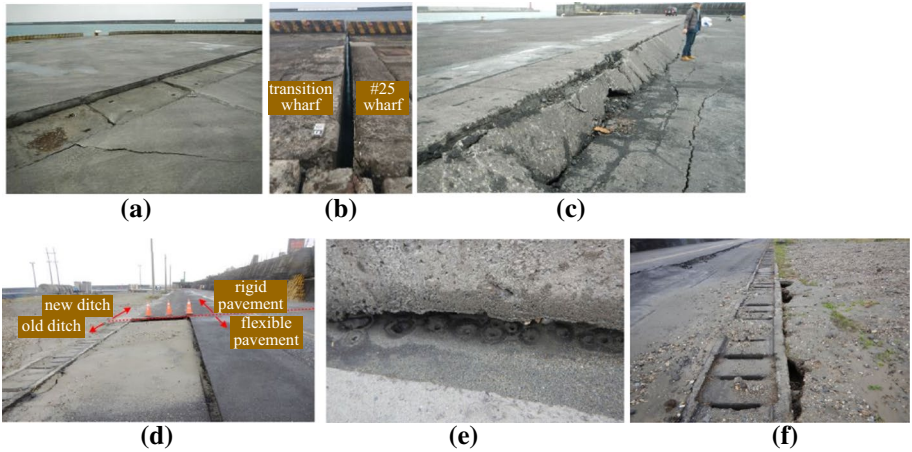


Fig. 29 a Differential settlement at wharf No. 25. b A gap between wharf No. 25 and the transition wharf. c Settlement at the back area of wharf No. 25. d The roads, e sand vents, and f hollowed roads and erupted mixtures on the western breakwater

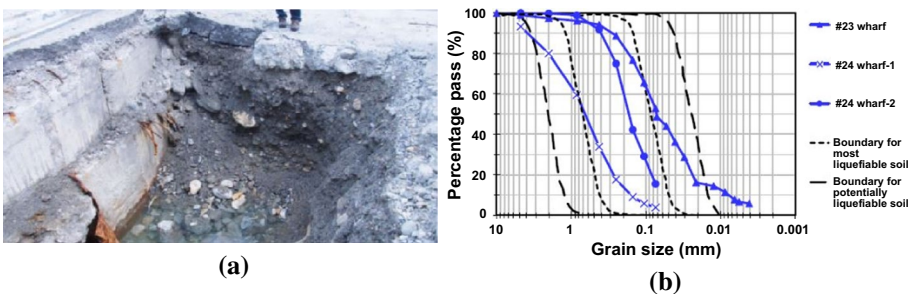


Fig. 30 a Excavated test pit. b Accumulation curves for grain sizes

shows the hollowed roads and the erupted mixtures caused by liquefaction at the western breakwater.

After the earthquake, Hualien Port Corporation excavated some test pits in the back areas to investigate the compositions of the backfill (Fig. 30). The test pits showed that the backfills are mixtures of large-size gravels, sands, and fine particles that are similar to those found in the settled back areas of CentrePort in New Zealand after the Kaikoura earthquake, 2016 (Cubrinovski et al. 2017). The grain sizes of the erupted mixtures during soil liquefaction at wharfs No. 23 and No. 24 were further analyzed (Hsu et al. 2018). Figure 30b shows the accumulation curves for the grain sizes. According to the unified soil classification system (Casagrande 1952), the erupted mixtures collected at wharf No. 23 are classed as ML (Mud, Low plasticity). Additionally, the erupted mixtures collected at two places at wharf No. 24 are classed as SP (Sand, Poorly graded) and SM (Sand, Mud). In addition to the three accumulation curves for the grain sizes, the boundaries for potentially liquefiable and most liquefiable soils suggested by the Ports and Harbors Association of Japan (PHAJ 1999) are also illustrated in Fig. 30b. The diagram shows that all the erupted mixtures during liquefaction collected at wharfs No. 23 and No. 24 were in the range of potentially liquefiable soils (Fig. 30b). Moreover, because all the settlements of the back areas of wharfs No. 23 to No. 25 are less than 700 mm, the seismic damage levels of these wharfs, whose caissons showed no obvious sliding, inclination or structural damage, are categorized as Level I (i.e., useable level) according to the seismic design guidelines for port structures (PIANC 2001).

6 Summary and conclusions

The casualties and collapsed buildings caused by the Hualien earthquake (which was coincidentally exactly two years after a previous devastating earthquake in Taiwan) deepened people's awareness of the importance of seismic preparation and contingency response. The main characteristics of this seismic event were near-fault ground motions and damages to structures located close to the active faults. The findings of reconnaissance work by Taiwan's National Center for Research on Earthquake Engineering (NCREE) for this seismic event are summarized as follows:

1. Some of the ground motion records had high velocity pulses that reflect the features of near-fault ground motions. Additionally, the vertical components of ground accelerations accompanying large peak ground velocities were close to or even greater than their horizontal counterparts. This phenomenon might be caused by the effect of soil nonlinearity. The associated stipulations of seismic design codes for seismic-induced vertical loads need to be further scrutinized.
2. The locations of the structures that suffered severe damage in the seismic event are distributed along the sides of the Milun Fault. From the acceleration response spectra obtained from the strong motion stations around the severely damaged structures, the spectral accelerations at medium to long vibration periods are significantly higher than the design response spectra. The large spectral accelerations resulting from the effect of near-fault ground motions were perhaps one of the main factors causing the structural damage. Therefore, the seismic design of medium to high-rise buildings close to active faults should be comprehensively reviewed. A limit on construction of such buildings may be a possible alternative.

3. The four collapsed buildings had a common feature that their bottom stories were elevated open spaces used for lobbies or parking lots. Besides the poor construction and the large seismic demands imposed by the near-fault ground motions, the soft and/or weak bottom stories resulting from these open spaces could be one of the key factors causing the building collapses. Three types of building collapse, i.e., the knee-down, sit-down, and lie-down types, were observed from present and past earthquake events. The factors differentiating the collapse types of buildings is worth further study for developing measures of altering undesired collapse types or even reducing the occurrence of building collapse.
4. Because of the amplified spectral accelerations at medium to long vibration periods, the effectiveness of the base isolation system installed in the monitored hospital building at reducing the roof's horizontal accelerations appeared to be not very significant. This manifests that near-fault effects play a vital role in the design of base-isolated buildings.
5. The significant differential displacements of land surfaces on the two sides of the active faults where Qixingtang Bridge and Hualien Bridge crossed over the faults were identified. The girders and piers of the two bridges seemed not to be significantly damaged, whereas most of the observed seismic damages were in the bridge decks, expansion joints, and seismic stoppers. In addition to decreasing the inertial forces transmitted to the substructures, the relative movements between the girders and their supporting bearings might offset the large displacement demands. When bridges inevitably cross active faults, the seismic mechanisms and capacities of the bridges for accommodating possible large differential displacements on the two sides of the active faults should be determined.
6. Soil liquefactions in the back areas of some wharfs of Hualien Port and subsequent significant sedimentation of the backfills were observed. However, the caissons of the wharfs were not apparently damaged, slid, or inclined. Hualien Port was thus useable immediately after the Hualien earthquake. The backfills of the back areas of wharfs should be sufficiently compacted to prevent possible soil liquefactions that may impair the functionalities of wharfs.

Above all, the Hualien earthquake once again exposed the vulnerability of aged buildings with soft and/or weak bottom stories. In light of the satisfactory seismic performance of the school buildings after the implementation of the nationwide seismic retrofitting project, the NCREC is engaging in a seismic retrofitting project for publicly used, privately owned aged buildings. Because there are millions of such buildings across the country, the seismic retrofitting of such buildings are prioritized according to their degree of seismic risk. In addition, the project will start with a few exemplar buildings and then be gradually promoted across the country. The seismic retrofitting of these buildings is to be completed in multiple phases. With findings from the Hualien earthquake, the first-phase work focuses on eliminating the possible collapses of buildings with soft and/or weak bottom stories.

Acknowledgements The authors gratefully acknowledge the assistance of the team of Prof. Yao, G.C. of the National Cheng Kung University, the Central Weather Bureau, the Hualien Tzu Chi Hospital, the Hualien Airport, and the Hualien Port, in addition to Assoc. Prof. Wang, K.L., of the National Chi Nan University. Special thanks are given to many other NCREC colleagues whose combined efforts helped complete the seismic reconnaissance.

References

- ASCE (2010) Minimum Design Loads for Buildings and other Structures. ASCE/SEI 7–10. American Society of Civil Engineers (ASCE), Reston, VA
- Casagrande A (1952) Electro-osmotic stabilization of soils. *Boston Soc Civ Eng J* 39(1):51–83
- CGS (2018) Geological survey report on 20180206 Hualien earthquake. Central Geological Survey, Ministry of Economic Affairs, Taiwan, R.O.C. (in Chinese)
- CICHE (2011) Application of design codes of concrete engineering. Civil 404–100, Chinese Institute of Civil and Hydraulic Engineering, Taipei, Taiwan (in Chinese)
- CPAMI (2011) Seismic design provisions and commentary for buildings. Construction and Planning Agency, Ministry of the Interior, Taiwan, R.O.C. (in Chinese)
- Cubrinovski M, Bray JD, de la Torre C, Olsen MJ, Bradley BA, Chiaro G, Stocks E, Wotherspoon L (2017) Liquefaction effects and associated damages observed at the Wellington centre port from the 2016 Kaikoura earthquake. *Bull N Z Soc Earthq Eng* 50(2):152–173
- Eurocode 8 (2003) Design of structures for earthquake resistance. Part1: General Rules, Seismic Actions and Rules for Buildings. prEN 1998–1:2003(E). Commission of the European Communities, European Committee for Standardization, Brussels
- Henry RS, Lee BY, McGuigan D, Finnegan J, Ashby G (2017) The 2016 Meinong Taiwan Earthquake: Learning from Earthquakes Report. *Bull N Z Soc Earthq Eng* 50(3):436–468
- Hsu SY, Yang HC, Lu CC, Hwang YW, Liu CH, Ko YY, Hwang JH (2018) The reconnaissance on seismic settlement of Hualien harbor and soil liquefactions in the 0206 Hualien earthquake. *Sino-Geotech* 156:65–76 (in Chinese)
- Hung HH, Chen CC, Su CK, Lee BH, Jang CL, Sung YC (2018) Reconnaissance observation and analysis on bridge damage caused by the 0206 Hualien earthquake. In: The 4th national conference on earthquake engineering, Taichung, Taiwan, 6–8 November, 2018. Paper No. 24014 (in Chinese)
- Hwang SJ, Chung LL, Chien WY, Hsiao FP, Chen HM, Shen WC, Yeh YK, Chuang CP (2012) Seismic upgrading project of public school buildings in Taiwan. *J Struct Eng* 27(1):4–16 (in Chinese)
- Jiang JH, Lin HC, Lin CC, Chen MY, Chung LL, Hwang SJ (2018) The school building reconnaissance report in 0206 Hualien earthquake. In: The 4th national conference on earthquake engineering, Taichung, Taiwan, 6–8 November, 2018. Paper No. 24003 (in Chinese)
- Kuo CH, Huang JY, Lin CM, Hsu TY, Chao SH, Wen KL (2019) Strong ground motion and pulse-like velocity observations in the near-fault region of the 2018 Mw 6.4 Hualien Taiwan earthquake. *Seismol Res Lett* 90(1):40–50
- Kuo CH, Lin CM, Chang SC, Wen KL, Hsieh HH (2017) Site database for Taiwan strong motion stations. Technical Report of National Center for Research on Earthquake Engineering, NCREE-17–004, 80 pp (in Chinese)
- Kuo CH, Wen KL, Hsieh HH, Lin CM, Chang TM, Kuo KW (2012) Site Classification and V_{S30} estimation of free-field TSMIP stations using the logging data of EGDT. *Eng Geol* 129–130:68–75
- Kwok OLA, Stewart JP, Kwak DY, Sun PL (2018) Taiwan specific model for V_{S30} prediction considering between-proxy correlations. *Earthq Spectra*. <https://doi.org/10.1193/061217EQS113M>
- Lin CM, Wen KL, Kuo CH, Lin CY (2014) S-wave velocity model of Taipei Basin. The 5th Asia Conference on Earthquake Engineering, Taipei, Taiwan, 16–18 October
- PHAJ (1999) Technical standards and commentaries for port and harbor facilities in Japan. The Ports and Harbors Association of Japan, Tokyo
- PIANC/International Navigation Association (2001) Seismic design guidelines for port structures. Balkema Publishers, Avereest
- Shahi SK, Baker JW (2014) An efficient algorithm to identify strong-velocity pulse in multicomponent ground motions. *Bull Seism Soc Am* 104(5):2456–2466
- Shen WC, Huang HW, Jiang JH, Weng PW, Chiou TC, Chung LL, Hwang SJ (2016) Investigation of seismic damage for school buildings affected by 0206 Meinong earthquake. In: The 3rd national conference on earthquake engineering, Taoyuan, Taiwan, 24–26 August, 2016. Paper No. 2303 (in Chinese)

Publisher's Note Springer Nature remains neutral with regard to jurisdictional claims in published maps and institutional affiliations.